applied optics

Active lens for thermal aberration compensation in lithography lens

Lei Zhao,[1,2,*] Lijian Dong,[1] Xinfeng Yu,[1,2] Pengzhi Li,[1,2] and Yanfeng Qiao[1]

[1]Changchun Institute of Optics, Fine Mechanics and Physics, Chinese Academy of Sciences, Changchun 130033, China
[2]University of Chinese Academy of Sciences, Beijing 100049, China
*Corresponding author: zhaolei1218@126.com

Received 9 July 2018; revised 13 September 2018; accepted 13 September 2018; posted 14 September 2018 (Doc. ID 338258); published 8 October 2018

High laser absorption and strong resolution enhancement technology make thermal aberration control of lithography lenses more challenging. We present an active lens that uses four bellows actuators to generate astigmatism (Z5) on the lens surface. The apparatus utilizes optical path difference to compensate the system wavefront. In order to assess the specifications of the compensator, the finite element method and experimental analyses are carried out to obtain and validate the general properties of the apparatus. The results show that the Z5 deformation quantity of lens's upper surface exceeds 600 nm; further, Z5 coefficient accuracy is better than ±1 nm. The apparatus can be an efficient compensator for thermal aberration compensation, especially aberration caused by the dipole illumination.

OCIS codes: (220.1080) Active or adaptive optics; (120.4880) Optomechanics; (120.6810) Thermal effects; (120.6650) Surface measurements, figure.

https://doi.org/10.1364/AO.57.008654

1. INTRODUCTION

Adaptive optics is used as an effective technology to improve the performance of imaging systems. It is widely applied in telescope systems [1,2], microscopy [3], visual optics [4], and lithography lenses [5]. Compared with conventional optical systems, adaptive optics systems use wavefront correctors to compensate aberration. These correctors can be separated into several types: deformable mirror [6], membrane deformable mirror [7], liquid crystal spatial light modulators [8], deformable liquid lens [9], and thermal optical element [10].

For a 193 nm lithography lens, higher-power laser sources are used to satisfy the ever-growing demand of throughput. As a result, the light power transmitted and absorbed in a lithography lens increases, thus heating the lens element. Meanwhile, off-axis illumination technology is used to enhance resolution. Such illuminations locally concentrate the light on the lens element. This concentration of power further aggravates a lens's thermal aberrations [11–13]. These make the thermal aberration control more challenging [14–16].

Lots of technologies for lens thermal aberration compensation have been developed, including lens manipulators, deformable mirrors, lens heating elements, and using low absorption glass materials. For example, Nikon developed an I-MAC system to adjust a lens element in z/tip/tilt directions; the system can control focus, distortion, spherical, coma, and other aberrations in real time [17]. Nikon further uses an infrared aberration control system to heat the lens pupil selectively; the system can correct uniform astigmatism caused by dipole-like illumination [18]. SVG developed an active deformable pupil mirror to compensate wavefront aberrations, such as astigmatism (Z5 and Z6) and trefoil (Z9 and Z10) [19]. Nikon applies quick reflex technology to the primary spherical mirror located near the lens pupil, so uniform astigmatism is perfectly compensated by deforming the mirror into a shape that opposes the astigmatism [20,21]. Nikon uses a multi-drive-axis dynamic deformable mirror to control the high-order wavefront with complex deformation of the mirror surface shape; the system can compensate for odd wavefront components [21,22]. ASML uses the FlexWave wavefront manipulator; the manipulator consists of an optical element positioned close to the pupil plane of the projection lens and is heated locally through tiny conductive and resistive structures. It can also adjust the Zernike coefficient up to 64 terms [23]. The Delft University of Technology developed an active mirror for extreme ultraviolet lithography lens compensation [24]. Low absorption glass and coating materials are selected to improve thermal aberration about 20%–30% [20]. These above technologies have been used in lithography lenses to improve thermal aberration. However, lens manipulators are limited to compensate on-axial aberration; deformable mirrors need more space to arrange actuators; lens heating elements are weak in rapid response; and using low absorption glass materials is just a passive compensation method.

In this paper, we present an active lens that uses four bellows actuators to generate astigmatism figures on the lens surface, utilizing the optical path difference (OPD) to generate a controlled wavefront. The designed Z5 active lens has a long deformable range (more than 600 nm) with high accuracy (less than 1 nm). The mechanism has high stiffness with a first frequency of 565.8 Hz and can respond rapidly. The apparatus is compact due to outside arrangement of actuators.

The paper is organized as follows. First, the principle of the deformable lens and the method of rigid motion error measuring are studied in Section 2. Section 3 then introduces the requirement and the main frame of the system and carries out simulation of the deformable lens and cell subsystem. Section 4 presents the testing of the system and experiments. Conclusions are drawn from the simulated and experimental results in Section 5.

2. PRINCIPLE OF THE Z5 ACTIVE LENS AND METHOD OF LENS RIGID MOTION TESTING

A. Z5 Active Lens Deformation Principle

As shown in Fig. 1, the lens is glued to the mounting cell through several flexural supporting rods. The cell is a monolithic structure with a fixed outer ring (not shown), deformable inner ring, and four connecting hinges. There are actuating legs between adjacent hinges. The input forces of the two actuating legs along the x axis act in the $-z$ direction, while those of the two actuating legs along the y axis act in the $+z$ direction. The four forces together result in a Z5 shape deformation.

B. Method of Measuring Lens Rigid Motion

Lens deformation of the Z5 shape will induce $z/x/y$/tip/tilt rigid motion error. Such errors should be tested first and then reduced to within a small range using control algorithms. The method of measuring and separating the deformed figure and rigid motion should therefore be studied first. This paper uses laser Fizeau interferometer to test for rigid motion error.

We use Fizeau interferometer to test for z axial rigid motion error ε_Z. Figure 2 shows the relationship between the axial rigid motion ε_Z and the wavefront defocus aberration (Z4).

The original wavefront can be expressed as

$$W_O(x,y) = \frac{x^2+y^2}{2(R-\varepsilon_Z)}. \tag{1}$$

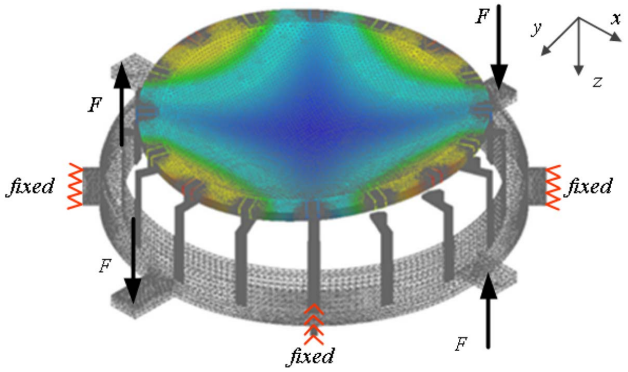

Fig. 1. Deformation principle of the Z5 active lens (where the outer ring is not shown).

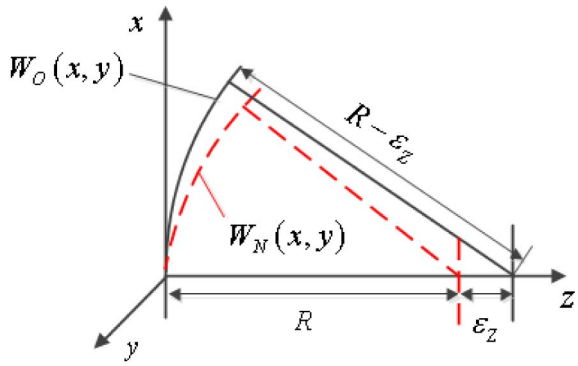

Fig. 2. Relationship between the axial rigid motion and wavefront defocus aberration (Z4).

The new wavefront can be expressed as

$$W_N(x,y) = \frac{x^2+y^2}{2R}. \tag{2}$$

The changed wavefront can thus be expressed as

$$\Delta W(x,y) = W_N(x,y) - W_O(x,y) = -\varepsilon_Z \frac{x^2+y^2}{2R^2}. \tag{3}$$

The axial rigid motion ε_Z can thus be calculated by first using a spherical interferometer to obtain the Z4 coefficient and then using Eq. (3).

To measure the x/y/tip/tilt rigid motion error of the lens's upper surface, we add a polished plane surface outside the upper surface. Using a Fizeau interferometer to measure the outer plane, we obtain the tip/tilt data. Then, changing the interferometer etalon to measure the inner spherical surface, we obtain the integrated x/y/tip/tilt data. Finally, employing a separating algorithm, the x/y/tip/tilt can be calculated individually. The algorithm is explained as follows.

When testing the spherical surface with a Fizeau interferometer, the surface tilt or shift will also change the Zernike coefficient Z2 (or Z3). Figure 3 shows the relationship between the surface tilt θ and Zernike Z2_tilt (or Z3_tilt). Z2_tilt (or Z3_tilt) refers to the Z2 (or Z3) caused by the surface tilt without any shift. The relationship is

$$\text{Z2\_tilt} = s \cdot \theta, \tag{4}$$

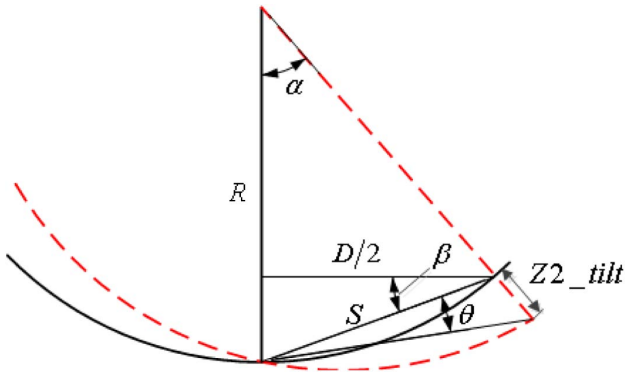

Fig. 3. Relationship between the surface tilt and Zernike Z2_tilt.

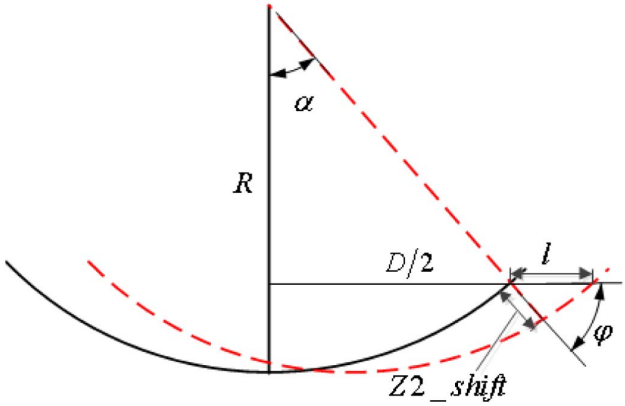

Fig. 4. Relationship between the surface shift and Zernike Z2_shift.

$$s = \frac{D}{2\cos\beta}. \tag{5}$$

The surface tilt and Zernike Z2 can be expressed as

$$\text{Z2\_tilt} = \frac{D}{2\cos\beta}\cdot\theta. \tag{6}$$

Figure 4 shows the relationship between the surface shift l and Zernike Z2_shift (or Z3_shift). The Z2_shift (or Z3_shift) refers to the Z2 (or Z3) caused by the surface shift without any tilt. The relationship is

$$\text{Z2\_shift} = l\cdot\cos\varphi, \tag{7}$$

$$\cos\varphi = \frac{D}{2R}. \tag{8}$$

The surface shift and Zernike Z2 can thus be expressed as

$$\text{Z2\_shift} = l\cdot\frac{D}{2R}. \tag{9}$$

When we test the upper spherical surface, Z2 is the combination of the Z2_tilt and Z2_shift:

$$\text{Z2} = \frac{D}{2\cos\beta}\cdot\theta + l\cdot\frac{D}{2R}. \tag{10}$$

When testing the outside plane surface, because plane shifting does not change the Z2 coefficient, Eq. (10) can be simplified as

$$\text{Z2} = \frac{D}{2}\cdot\theta. \tag{11}$$

The measuring strategy is as follows. We first measure the outside plane surface; according to the Z2 coefficient obtained, we can calculate the surface tilt rigid motion error θ. We then measure the inner spherical surface and obtain the Z2 coefficient. Using the Z2 coefficient and tilt rigid motion θ, we can calculate the surface shift rigid motion l.

3. DESIGN OF THE Z5 ACTIVE LENS SYSTEM

Figure 5 shows the general frame of the Z5 active lens. The Z5 active lens system can be separated into three subsystems: the mounting cell and lens subsystem, the actuator subsystem (comprising the actuator bellows, capacitance displacement sensors, and pneumatic valve) and the control subsystem.

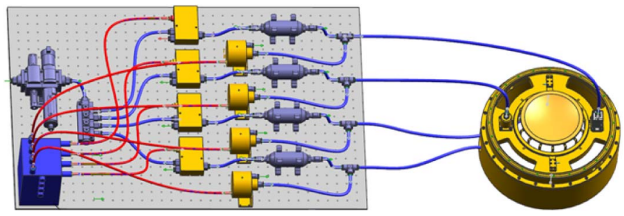

Fig. 5. General frame of the Z5 active lens system.

A. Requirements of the Z5 Active Lens System

Requirements of the Z5 active lens system include the range, accuracy, figure residual error, rigid motion error, and natural frequency. Range, accuracy, and coupling errors are based on the deformation of the upper surface of the lens element at the maximum clear aperture. The above parameters are listed in Table 1.

The range and accuracy of the deformable lens depend on the thermal aberration and the sensitive matrix between the deformable lens' upper surface figure and system wavefront aberration. Unlike the deformable mirror, the upper surface and the lower surface of the lens will deform together; different is the quantity, and thus the lens requires more deforming range than the mirror. In a lithography system, as shown in Fig. 6, lens 8 is selected as a Z5 active lens. Under the condition of annular illumination, the thermal-caused Z5 coefficient of wavefront aberration is about 25 nm. The relationship between wavefront Z5 and upper surface Z5 is shown in Fig. 7. Figure 7(a) shows the input upper surface figure, and the Z5 coefficient is 600 nm. Figure 7(b) shows the corresponding lower surface figure, and the Z5 coefficient is 616 nm. Figure 7(c) shows the output wavefront aberration when the upper and lower surface figures are added. The Z5 coefficient is 24.6 nm, and the ratio of the upper surface Z5 to wavefront Z5 is 24.4. Thus, the wavefront Z5 accuracy is 0.25 nm. Figure 7(d) shows the corresponding wavefront aberration when the upper and lower figures and x/y/tip/tilt rigid

Table 1. Requirements of the Z5 Active Lens System

Parameters	Requirement
Range	600 nm
Accuracy	6 nm
z Rigid motion error	100 nm
x/y/tip/tilt rigid motion errors	500 nm/500 ms
Figure error (≥Z6, except Z12)	1 nm (RMS)
Natural frequency	400 Hz

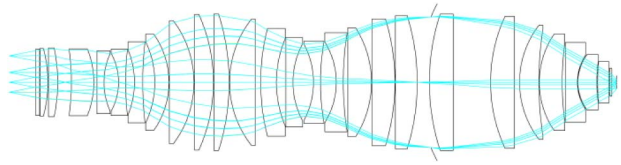

Fig. 6. Lithography lens.

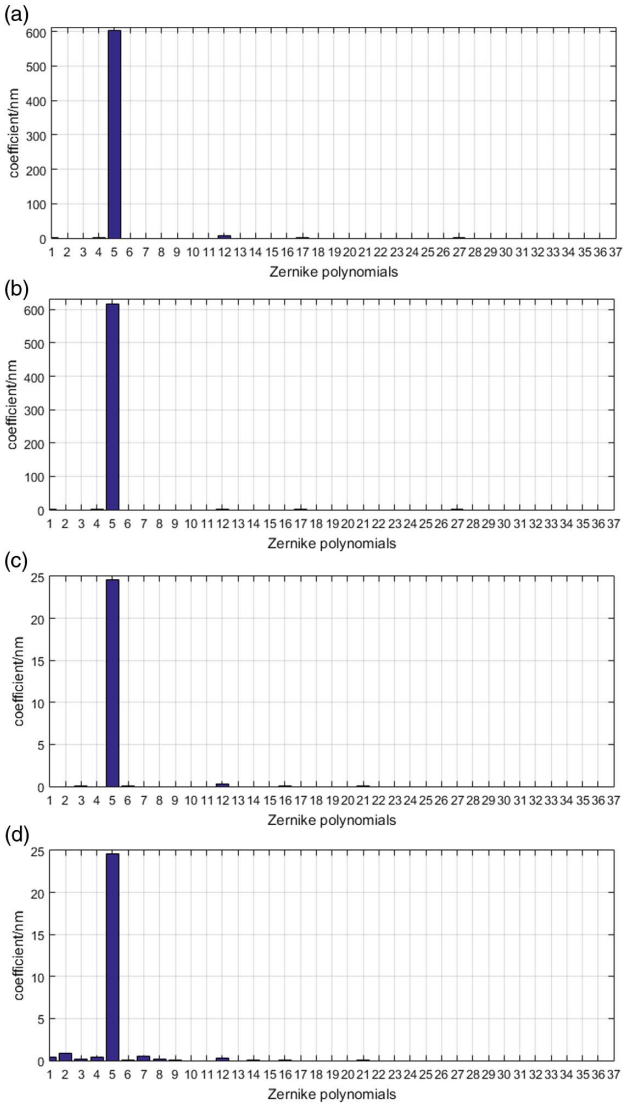

Fig. 7. Relationship between upper surface Z5 and wavefront Z5. (a) Input upper surface figure data. (b) Corresponding lower surface figure data. (c) Output wavefront aberration caused by surface deformation. (d) Output wavefront aberration caused by surface deformation and coupling rigid motion errors.

motion errors are added. Coupling rigid motion errors will cause wavefront aberrations such as Z1, Z2, Z3, Z4, Z7, and Z8. The quantity is very little, and the RMS wavefront error (except Z5 and Z12) is less than 0.5 nm. The coupling wavefront errors can be controlled even smaller, though working together with other compensators such as Z-axis lens manipulators and reticle/wafer manipulators.

B. Design and Simulation of the Lens and Cell Subsystem

Figure 8 shows the lens and cell subsystem. The coordinate system is defined as follows. The Z axis is parallel to the light direction and lies on the center line of the optical path of the lens. The X axis and Y axis pass through the vertex of the upper surface of the lens. The lens diameter is 160 mm and the clear aperture is 130 mm, while the lens center thickness is 19 mm.

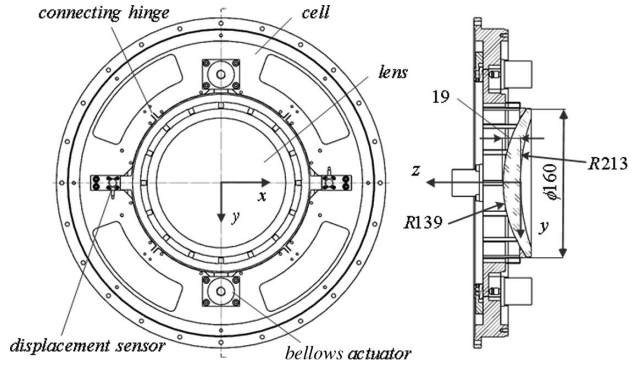

Fig. 8. Cell and lens subsystem.

The upper and lower surface radiuses are, separately, 213 and 139 mm. The mounting cell is a monolithic structure and can be separated into an outer ring, deformable inner ring, and four connecting hinges; the cell can be precision manufactured employing wire electrical discharge machining. The deformable inner ring has several flexural supporting rods that can also be manufactured by wire electrical discharge machining. The deformable lens is located on the flexural supporting rods. The supporting rods have axial and radial flexure and can reduce the stress transmitted to the lens and realize high figure accuracy of the lens surface. Making the subsystem with high rigidity, we use Norland optical adhesive 61 to glue the lens and cell. The bellows actuator is fixed on the cell's outer ring. In operation, the bellows head strikes and deforms the cell inner ring. In the opposite direction of the bellows, there is a capacitance position sensor that detects the cell's inner ring displacement in real-time.

Figure 9 shows a model of the Z5 active lens. This model is used to simulate the deformation range, induced figure error, and the induced rigid motion error. To simplify the model and improve the simulation efficiency, we removed the cell's outer ring. The four connecting hinges are fixed constraints. Four groups of force/enforced displacement are applied on the arm of the cell's inner ring. The direction of the force/enforced displacement applied on the two arms of the X axis is along the $-Z$ axis, while the direction of the force/enforced displacement

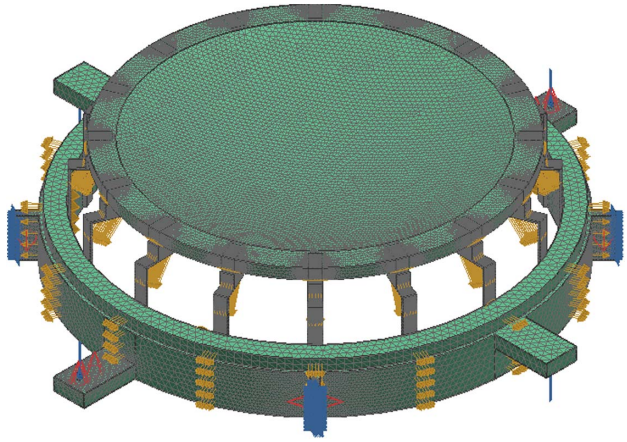

Fig. 9. Model of the Z5 active lens.

Table 2. Main Parameters of Fused Silicon, 430F, and Norland 61

Material	Young's Modulus (Gpa)	Poisson Ratio	Density (kg/m^3)	Yield Strength (Mpa)
Fused Silicon	73	0.17	2205	50
430F	200	0.27	7700	450
Norland 61	0.93	0.35	1290	19.3

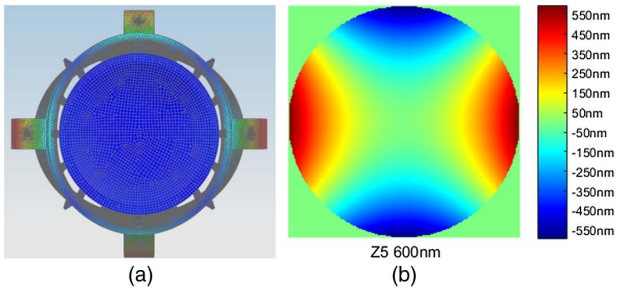

Fig. 10. Simulation result of the Z5 active lens. (a) Deformation of the cell and lens. (b) Deformation of the upper surface.

applied on the two arms of the Y axis is along the $+Z$ axis. Faces are glued to connect the flexural supporting rods of the inner ring and lens; the area of the glue is equal to the size of the head area of the flexural supporting rods, and the glue layer thickness of the connecting area is about 10 μm.

Materials of the lens, cell, and glue are separately fused silicon, 430F, and Norland61. The main parameters of these materials are listed in Table 2.

Figure 10 shows the simulation results. Figure 10(a) shows the deformation of the cell and lens subsystem when a force/enforced displacement is applied. Figure 10(b) shows the deformation of the upper surface. The Z5 coefficient of the upper surface is 600 nm (where the figure is 1200 nm PV, 240 nm RMS), while the input force is 76.67 N or the enforce displacement is 25.78 μm. When the upper surface Z5 coefficient is 600 nm, the induced maximum stresses of the lens and glue are, respectively, 2.318 and 3.511 MPa. Considering the allowed strength of 50 MPa (fused silicon) and 19.3 MPa (Norland 61), the safety factor is high. The Z5 deformation quantity of the lens's upper surface therefore exceeds 600 nm.

Figure 11 shows data for the induced figure. Figure 11(a) shows the corresponding Z12 coefficient. The corresponding Z12 coefficient is 9.742 nm, while the Z5 coefficient is 600 nm. Figures 11(b) and 11(c) show the induced figure error and corresponding individual Zernike coefficient. The induced figure error (≥$Z6$, except sec-astigmatism Z12) is 0.11 nm root mean square (RMS), while the Z5 coefficient is 600 nm. The main components are astigmatism 45 deg. (Z6), quatrefoil (Z17), and ter-astigmatism Z21.

Modal analysis of the active lens is carried out. Figure 12 shows the first six modes of vibration. The corresponding first six natural frequencies are 565.8, 566, 643.8, 725.8, 784, and 824 Hz.

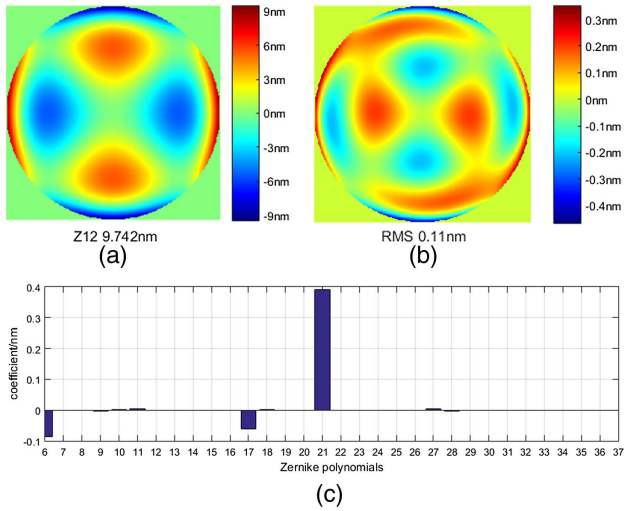

Fig. 11. Z12 coefficient and figure residual error (≥Z6, except Z12). (a) Z12 coefficient. (b) Figure error (≥ Z6, except Z12). (c) Individual Zernike coefficient (≥Z6, except Z12).

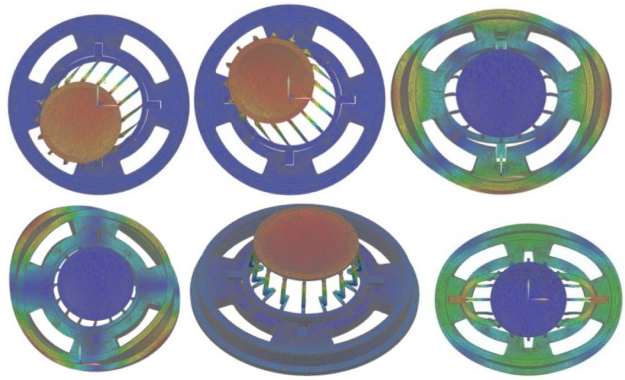

Fig. 12. First six modes of vibration.

C. Actuator Subsystem

The actuator subsystem contains the actuator bellows, pressure sensor, and pneumatic valve. According to the simulated results, the actuator subsystem should have an output force exceeding 76.67 N and a good linear quality of the full range. Meanwhile, the simulated result shows that the needed enforce displacement is 25.78 μm, and the initial gap between the bellows head and the cell should be considered, such that the whole range of the bellows is better than 1 mm.

The principle of the bellows actuator is shown in Fig. 13. The output force F_{out} and the input pressure P_{in} can be expressed as

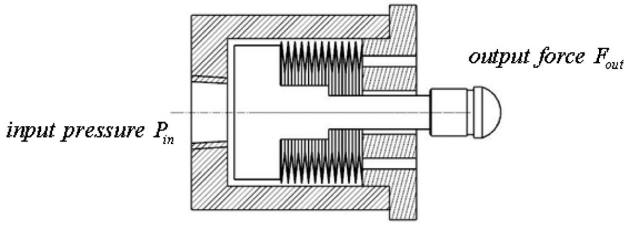

Fig. 13. Principle of the bellows actuator.

$$F_{\text{out}} = P_{\text{in}} \cdot S_e, \tag{12}$$

wherein S_e is the effective area of the bellows, which is 182.4 mm^2 for the selected bellows.

We choose a Chunk DS15R as the pneumatic valve. The main parameters are as follows. The output pressure range is 600 kPa, the output pressure resolution is 1.4 kPa, the output pressure linearity is 1% of the full range, and the response time for pressurization from 0 to 5 bars is 40 ms, while the response time for depressurization from 6 to 1 bar is 54 ms. We choose a Setra 204D as the pressure sensor. The range is up to 100 PSI, the accuracy is 0.11% of the full range, and the response time is less than 1 ms. The output range and resolution of the actuator subsystem depend on the bellows, pressure valve, and sensor. The maximum output force is about 110 N, and the resolution of the output force is about 0.26 N.

4. EXPERIMENT ON THE Z5 ACTIVE LENS SYSTEM

A. Experimental Platform

Figure 14 shows the experimental platform of the Z5 active lens system. The experimental platform comprises an xPC control subsystem, actuator subsystem, deformable cell/lens subsystem, and Fizeau interferometer. The Fizeau interferometer is used to test the Z5 range, accuracy, figure residual error, and rigid motion error.

Figure 15 shows the control frame of the Z5 active lens. The experiment is based on the xPC real-time platform. The output

Fig. 14. Experimental platform of the Z5 active lens system.

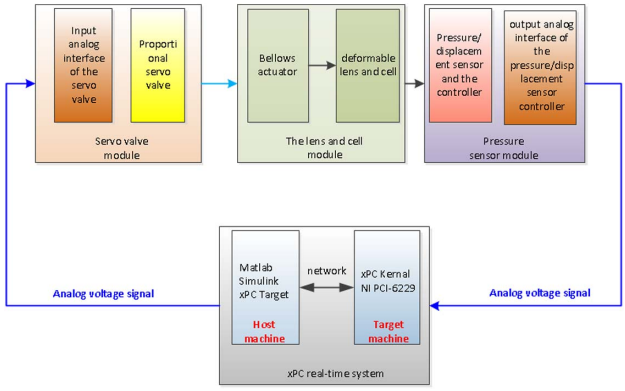

Fig. 15. Control frame of the Z5 active lens.

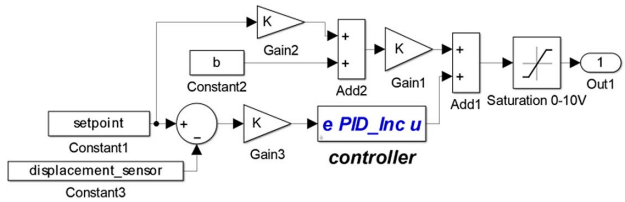

Fig. 16. Control strategy.

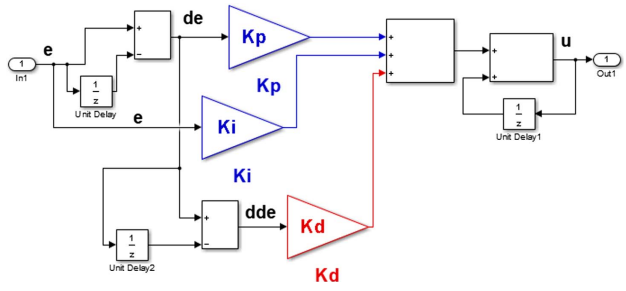

Fig. 17. PID control module.

analog signal of the xPC platform is sent to the pneumatic servo-valve. The adjusted pressure is connected to the bellows and deforms the cell and lens. The displacement sensors measure output displacements of the bellows. The sensors' analog signals are then sent back to the xPC real-time platform. MATLAB/Simulink software is used to establish the control model and strategy, while code is generated through the real-time workshop.

Figures 16 and 17, respectively, show the control strategy and proportional–integral–derivative (PID) control module. The label e denotes the deviation between the target and real values, while u denotes the output voltage after PID calibration.

B. Experiment on the Z5 Active Lens (Displacement Closed Loop)

Using the experimental platform, we obtain the input displacement and output Zernike coefficient Z2/Z3/Z4/Z5. We then calculate the transition matrix. Using the transition matrix, we measure the range, resolution, accuracy, figure residual error, and rigid motion error. Figure 18 shows a prototype of the

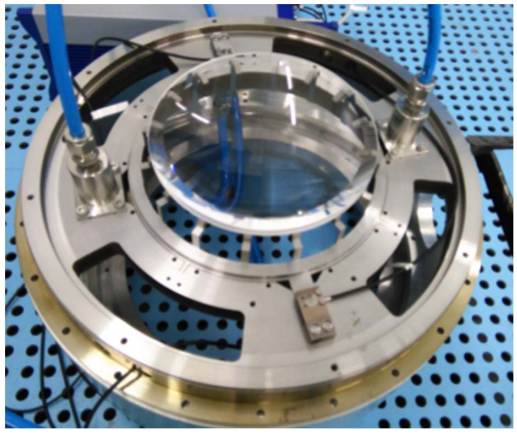

Fig. 18. Prototype of the Z5 active lens.

Z5 active lens. Displacement sensors are located in the opposite direction of the bellows for feedback.

The transition matrix of the system is studied first. The input is the displacements of the four position sensors. The output is the Zernike coefficients Z2, Z3, Z4, and Z5. Figures 19–22 show the relationship among the Z2, Z3, Z4, and Z5 coefficients and the four input displacements, respectively. Px, Nx, Py, and Ny in these figures, respectively, refer to the displacements actuated in the +X, –X, +Y, and –Y regions of the inner cell.

According to the experimental data, the matrix for the transition between the four input displacements and the Zernike coefficients Z2, Z3, Z4, and Z5 can be expressed as

$$\begin{bmatrix} Z_2 \\ Z_3 \\ Z_4 \\ Z_5 \end{bmatrix} = \begin{pmatrix} 100.98 & -107.93 & -3.62 & 3.14 \\ -8.25 & 13.28 & -97.23 & 89.50 \\ -1.29 & -1.37 & 1.34 & 1.24 \\ 6.27 & 6.41 & 6.11 & 6.07 \end{pmatrix} \begin{bmatrix} P_x \\ N_x \\ P_y \\ N_y \end{bmatrix}. \quad (13)$$

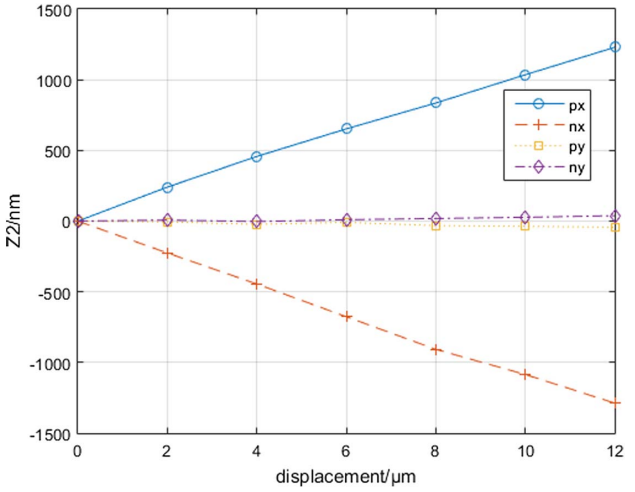

Fig. 19. Relation between Z2 coefficient and input four displacements.

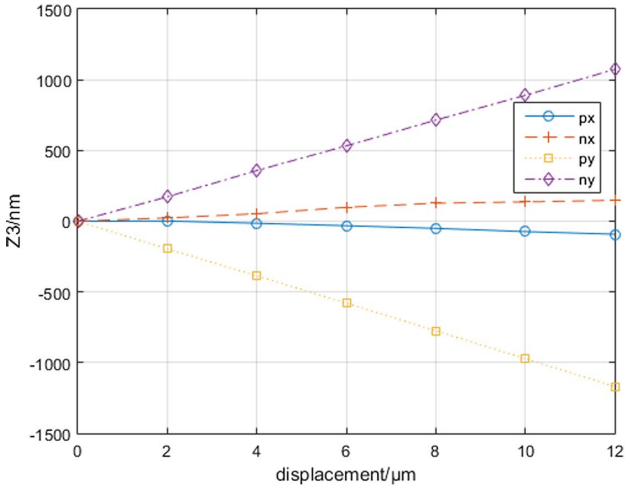

Fig. 20. Relation between Z3 coefficient and input four displacements.

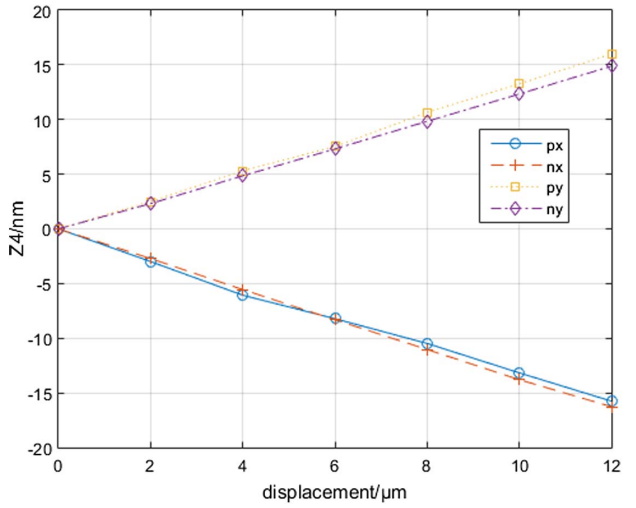

Fig. 21. Relation between Z4 coefficient and input four displacements.

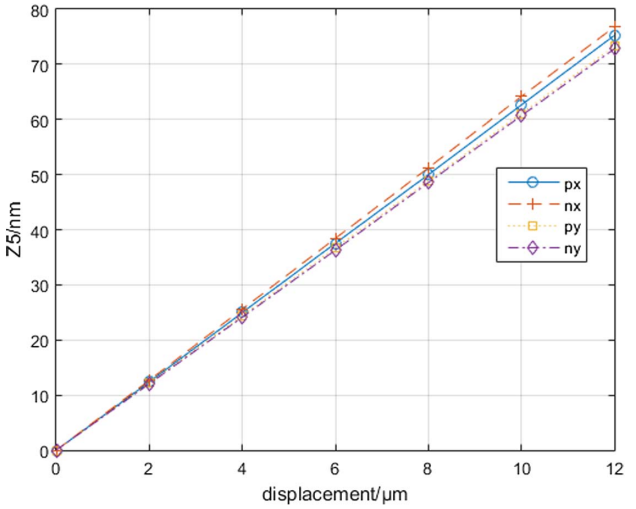

Fig. 22. Relation between Z5 coefficient and input four displacements.

According to Eq. (13), the system is sensitive to Z2 and Z3, and we should thus pay much attention to the manufacturing accuracy of the cell, especially the four hinges, and the assembly accuracy of the four actuators. The matrix can be micro-adjusted by changing the positions of the four actuators. We can use the matrix to reduce the Z2, Z3, and Z4 errors. For example, we can set $Z2 = 0$, $Z3 = 0$, $Z4 = 0$, and $Z5 = 600$ and obtain the needed actuator inputs Px, Nx, Py, and Ny.

The range of the Z5 active lens depends on the input force/displacement, the stiffness and strength of the system. Figure 21 shows the Z5 range of the system. Figure 23(a) shows the initial figure data of the upper surface of the lens. Figure 23(b) shows the figure data of the upper surface of the lens for maximum displacement actuated in the +X, –X, +Y, and –Y regions. Figure 23(c) shows the figure data of the difference between the maximum displacement and the initial displacement; this is the deformable range of the Z5 coefficient, which is 735 nm.

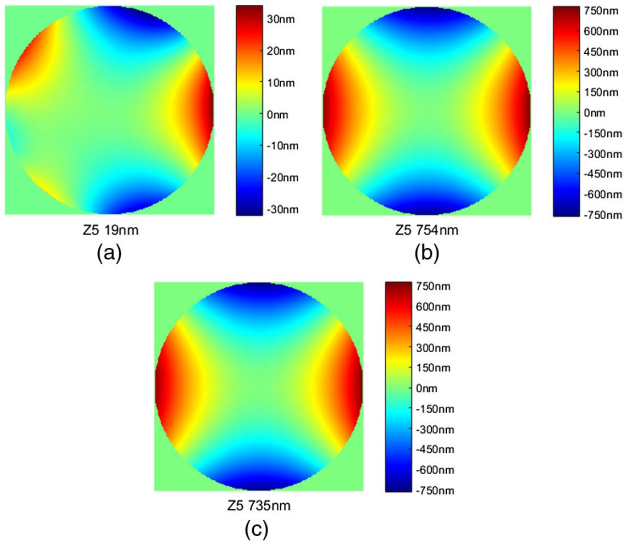

Fig. 23. Z5 deformable range of the system. (a) Initial surface figure data. (b) Surface figure data after deforming. (c) Changing of surface figure data.

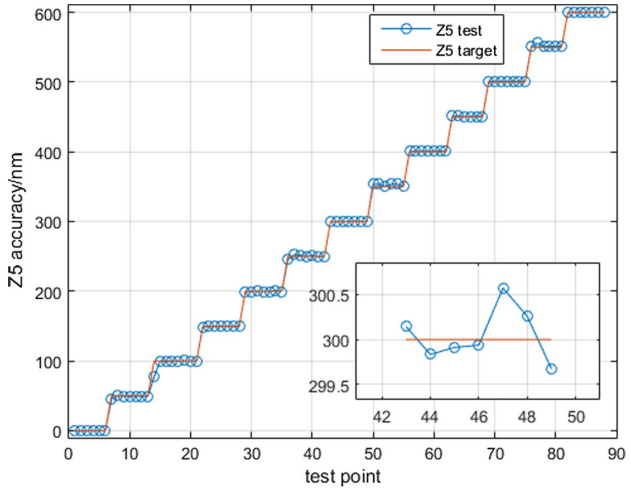

Fig. 24. Accuracy of Z5 active lens.

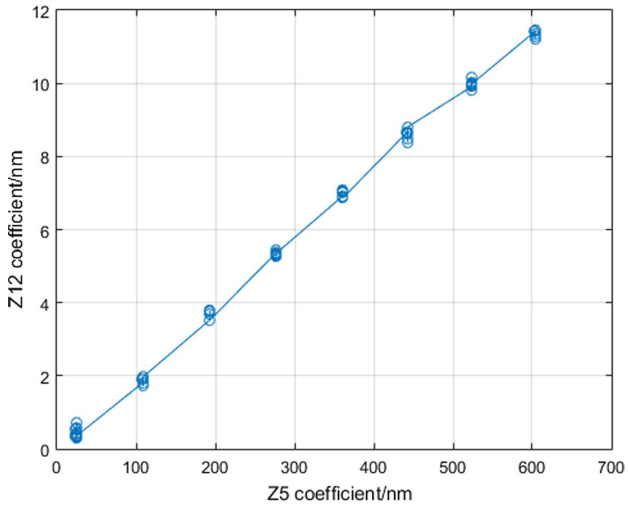

Fig. 25. Z12 coefficient with an increase in the Z5 coefficient.

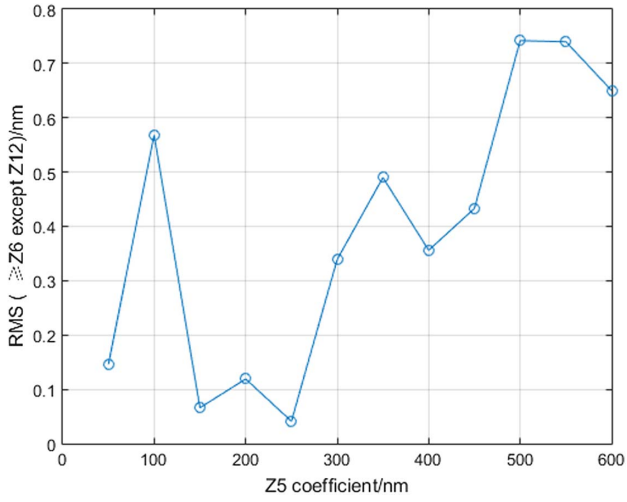

Fig. 26. Induced figure residual error.

Accuracy is defined as the difference between the actual astigmatism and target astigmatism. When the target astigmatism is known, we can calculate the input displacement using the transition matrix in Eq. (13), and the actual astigmatism can then be experimentally investigated. Figure 24 shows the experimental results of the accuracy with the Z5 coefficient increasing in steps of 50 nm. Measurements are made at about seven points for each step, and the Z5 error is found to be less than ± 1 nm.

Figure 25 shows the Z12 coefficient with an increase in the Z5 coefficient. The Z12 coefficient error is a maximum of 11.216 nm when the Z5 coefficient is 600 nm. The experimental result is only a little greater than the simulation result. The relative error of 13% is mainly due to manufacturing error of the deformable cell, the lens and cell bonding inhomogeneity, and the assembly error of the actuators. The Z12 coefficient is proportional to the Z5 coefficient, with the linear coefficient being 0.0192. The proportionality is a constant that mainly depends on the lens geometry and material. Therefore, when selecting a deformable lens for the lithography system, the Z5 and Z12 coefficients of the lens figure error should be considered together. In practice, the Z5 and Z12 coefficients of the upper and lower surfaces will add to the system, and the system wavefront aberration based on the Zernike coefficient can be calculated. The matrix of sensitivity between the system coefficient and the figure error can be calculated. Owing to the dipole and quadrupole illumination, the heat-induced system aberration also contains large Z5 and Z12 components. Therefore, when selecting the deformable lens, we should consider the system aberration, sensitive matrix, and Z5/Z12 proportional relation of the lens figure.

The induced figure residual error (≥Z6, except Z12) is shown in Fig. 26. The figure error is stochastic; the quantity is less than 0.8 nm root mean square (RMS), and the measuring

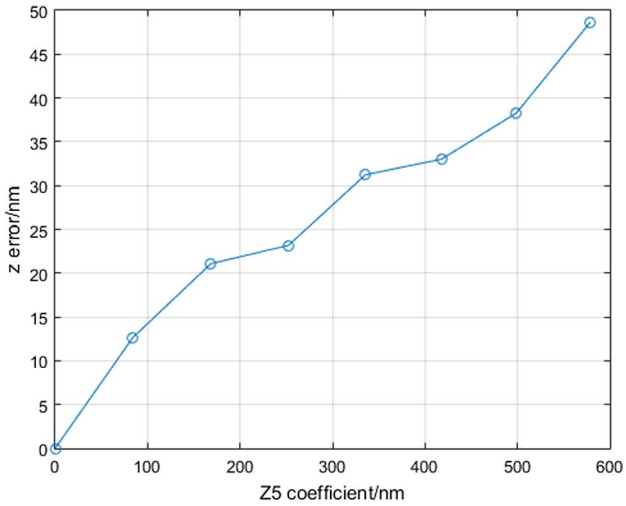

Fig. 27. Z-axial rigid motion error of the upper surface.

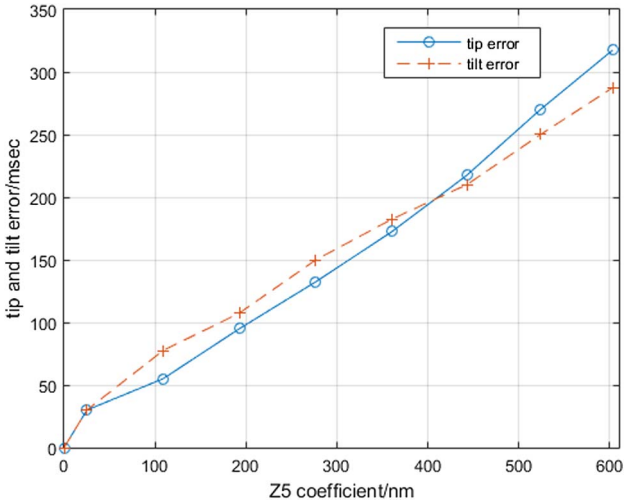

Fig. 28. Tip and tilt rigid motions of the upper surface.

error caused by the environment fluctuation is the main error source.

Using Eq. (3), we can obtain the z-axial rigid motion when we test the defocus (Z4 coefficient). Figure 27 shows the corresponding z-axial rigid motion error as the input Z5 coefficient (astigmatism) changes. To eliminate the effect of the random difference, we repeat the test several times and use the average data. The z-axial rigid motion error is a maximum of 50 nm when the deformable Z5 coefficient is 600 nm.

We measure the Z2 and Z3 coefficient of the upper spherical surface and the outside plane surface. Then, using the algorithm expressed by Eqs. (10) and (11), we obtain the lens upper surface x/y/tip/tilt rigid motion error. Figure 28 shows the tip/tilt rigid error measured with the plane etalon. The tip and tilt rigid motion errors are separately 317.5 and 287.5 msec when the Z5 coefficient is 600 nm. Figure 29 shows the x/y rigid error measured using plane and spherical etalons.

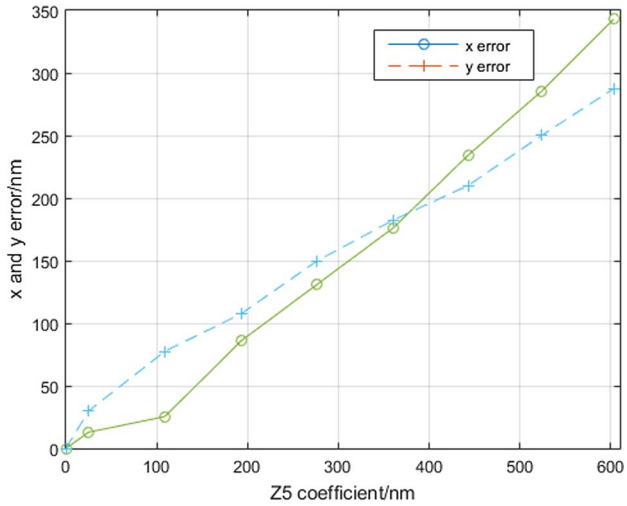

Fig. 29. X- and y-axis rigid motions of the upper surface.

The x- and y-axis rigid motion errors are, separately, 342.9 and 223.5 nm when the Z5 coefficient is 600 nm.

5. CONCLUSION

The paper presented a prototype of the Z5 active lens. The lens Z5 deformable principle and the method of rigid motion error testing were introduced, as were the main frame and the requirements of the system. Simulations and experiments were carried out to evaluate the system. The simulation results are as follows. The Z5 deformation quantity of the lens's upper surface exceeds 600 nm. The first six natural frequencies are 565.8, 566, 643.8, 725.8, 784, and 824 Hz. The following experimental results were obtained. The accuracy is better than ± 1 nm. The figure error ($\geq$Z6, except Z12) is less than 0.8 nm root mean square (RMS) when the Z5 coefficient is 600 nm. The $z/x/y$/tip/tilt rigid motion errors are 50 nm/342.9 nm/223.5 nm/317.5 msec/287.5 msec, respectively, when the deformable Z5 coefficient is 600 nm. The simulated and experimental results show that the Z5 active lens can satisfy technical requirements and can be used effectively for the compensation of the thermal aberration of a lithography lens.

For a real active lens used in a projection lens, the specifications of range, accuracy, and coupling errors depend on the sensitivity matrix to the system aberration, and the system compensation strategy. The selected active lens may therefore have longer range and stricter coupling specifications. Future work is needed to research a sensitive matrix between lens upper surface figure and system aberration. Continuous research is also needed to improve measuring accuracy and control coupled rigid motion errors. Measuring x/y/tip/tilt simultaneously without changing the interferometer etalon should be carried out to improve the accuracy of measuring rigid motion. As an example, we will apply a special type of computer-generated holography to generate plane and spherical waves simultaneously. To control the coupled rigid motion, the effect of manufacturing and assembly error should be considered; advanced control strategy should also be used.

Funding. National Youth Foundation of China (61504142).

Acknowledgment. We thank the Changchun Institute of Optics, Fine Mechanics and Physics for the use of its equipment.

REFERENCES

1. N. Devaney, F. Kenny, A. V. Goncharov, M. Goy, and C. Reinlein, "Development of a prototype active optics system for future space telescopes," Appl. Opt. **57**, E101–E106 (2018).
2. E. Segato, V. D. Deppo, S. Debei, G. Naletto, G. Cremonese, and E. Flamini, "Method for studying the effects of thermal deformations on optical systems for space application," Appl. Opt. **50**, 2836–2845 (2011).
3. B. Potsaid, Y. Bellouard, and J. T. Wen, "Adaptive scanning optical microscope (ASOM): a multidisciplinary optical microscope design for large field of view and high resolution imaging," Opt. Express **13**, 6504–6518 (2005).
4. E. J. Fernández and P. Artal, "Membrane deformable mirror for adaptive optics: performance limits in visual optics," Opt. Express **11**, 1056–1069 (2003).
5. R. Saathof, G. J. M. Schuttena, J. W. Spronckа, and R. H. M. Schmidt, "Design and characterisation of an active mirror for EUV-lithography," Precis. Eng. **41**, 102–110 (2015).
6. M. Zhang, L. Zhao, L. J. Dong, Y. X. Sui, and H. J. Yang, "A deformable plane-parallel optical plate with 16 actuated points for low order aberrations correction," Proc. SPIE **9686**, 968605 (2016).
7. S. Nam, S. Park, S. Yun, B. Park, S. K. Park, and K. U. Kyung, "Structure modulated electrostatic deformable mirror for focus and geometry control," Opt. Express **24**, 55–66 (2016).
8. K. N. Yao, J. L. Wang, X. Y. Liu, and W. Liu, "Closed-loop adaptive optics system with a single liquid crystal spatial light modulator," Opt. Express **22**, 17216–17226 (2014).
9. N. C. Lima, K. Mishra, and F. Mugele, "Aberration control in adaptive optics: a numerical study of arbitrarily deformable liquid lenses," Opt. Express **25**, 6700–6711 (2017).
10. H. Chen, L. Hou, and X. L. Zhou, "Active compensation of wavefront aberrations by controllable heating of lens with electric film heater matrix," Appl. Opt. **55**, 6634–6638 (2016).
11. X. F. Yu, M. Y. Ni, D. Rui, Y. Qu, and W. Zhang, "Computational method for simulation of thermal load distribution in a lithographic lens," Appl. Opt. **55**, 4186–4191 (2016).
12. C. C. Yao and Y. Gong, "Simulation research on the thermal effects in dipolar illuminated lithography," J. Opt. Soc. Korea **20**, 251–256 (2016).
13. H. Chen, H. J. Yang, X. F. Yu, and Z. G. Shi, "Simulated and experimental study of laser-beam-induced thermal aberrations in precision optical systems," Appl. Opt. **52**, 4370–4376 (2013).
14. T. Yoshihara, T. Sukegawa, N. Yabu, M. Kobayashi, T. Arai, T. Kitamura, A. Shigenobu, Y. Hasegawa, and K. Takahashi, "Advanced aberration control in projection optics for double patterning," Proc. SPIE **7274**, 72741 (2009).
15. T. Funatsu, Y. Uehara, Y. Hikida, A. Hayakawa, S. Ishiyama, T. Hirayama, H. Kono, Y. Shirata, and Y. Shibazaki, "Latest performance of ArF immersion scanner NSR-S630D for high-volume manufacturing for 7 nm node," Proc. SPIE **9426**, 942617 (2015).
16. V. V. Zelenogorsky, A. A. Solovyov, I. E. Kozhevatov, E. E. Kamenetsky, E. A. Rudenchik, O. V. Palashov, D. E. Silin, and E. A. Khazanov, "High-precision methods and devices for in situ measurements of thermally induced aberrations in optical elements," Appl. Opt. **45**, 4092–4101 (2006).
17. T. Nakashima, Y. Ohmura, T. Ogata, Y. Uehara, H. Nishinaga, and T. Matsuyama, "Thermal aberration control in projection lens," Proc. SPIE **6924**, 69241 (2008).
18. Y. Uehara, T. Matsuyama, T. Nakashima, Y. Ohmura, T. Ogata, K. Suzuki, and N. Tokuda, "Thermal aberration control for low k1 lithography," Proc. SPIE **6520**, 65202V (2007).
19. H. Sewell, J. A. McClay, A. Guzman, and C. Lafiandra, "Aberration control for 70-nm optical lithography," Proc. SPIE **4404**, 279–290 (2001).
20. Y. Ohmura, T. Ogata, T. Hirayama, T. I. Shiota, S. Ishiyama, S. Isago, H. Kawahara, and T. Matsuyama, "An aberration control of projection optics for multi-patterning lithography," Proc. SPIE **7973**, 79730W (2011).
21. Y. Ohmura, Y. Tsuge, T. Hirayama, H. Ikezawa, D. Inoue, Y. Kitamura, Y. Koizumi, K. Hasegawa, S. Ishiyama, T. Nakashima, T. Kikuchi, M. Onda, Y. Takase, A. Nagahiro, S. Isago, and H. Kawahara, "High-order aberration control during exposure for leading-edge lithography projection optics," Proc. SPIE **9780**, 97800Y (2016).
22. Y. Yoda, A. Hayakawa, S. Ishiyama, Y. Ohmura, I. Fujimoto, T. Hirayama, Y. Shiba, K. Masaki, and Y. Shibazaki, "Next-generation immersion scanner optimizing on-product performance for 7 nm node," Proc. SPIE **9780**, 978012 (2016).
23. F. Staals, A. Andryzhyieuskaya, H. Bakker, M. Beems, J. Finders, T. Hollink, J. Mulkens, A. Nachtwein, R. Willekers, P. Engblom, T. Gruner, and Y. Zhang, "Advanced wavefront engineering for improved imaging and overlay applications on a 1.35 NA immersion scanner," Proc. SPIE **7973**, 79731 (2011).
24. R. Saathof, G. J. M. Schutten, J. W. Spronck, and R. H. M. Schmidt, "Actuation profiles to form Zernike shapes with a thermal active mirror," Opt. Lett. **40**, 205–208 (2015).